The Combined Link of the Indian Ocean Dipole and ENSO with the North Atlantic–European Circulation during Early Boreal Winter in Reanalysis and the ECMWF SEAS5 Hindcast

ALESSANDRO RAGANATO,[a,b] MUHAMMAD ADNAN ABID,[c,b] AND FRED KUCHARSKI[b]

[a] *School of Earth and Atmospheric Sciences, Georgia Institute of Technology, Atlanta, Georgia*
[b] *Earth System Physics, The Abdus Salam International Centre for Theoretical Physics, Trieste, Italy*
[c] *Atmospheric, Oceanic and Planetary Physics, Department of Physics, University of Oxford, Oxford, United Kingdom*

(Manuscript received 23 November 2023, in final form 12 September 2024, accepted 14 September 2024)

ABSTRACT: During early boreal winter, the extratropical atmospheric circulation is influenced by Rossby waves propagating from the Indian Ocean toward the North Atlantic–European (NAE) regions, resulting in a North Atlantic Oscillation (NAO)-like pattern. The mechanisms driving these teleconnections are not well understood and are crucial for improving model skills. This study investigates these mechanisms using the ERA5 dataset and tests the predictive capabilities of the ECMWF SEAS5, exploring potential reasons for a weak model response. Linear regression methods are employed to examine the extratropical links with the Indian Ocean dipole (IOD), both in isolation and in combination with El Niño–Southern Oscillation (ENSO). Our findings demonstrate a connection between October IOD sea surface temperature anomalies and December Indian Ocean precipitation patterns. Furthermore, a correlation between the October IOD and December NAO time series suggests a link between the IOD and NAE circulation. The early winter European response to a positive IOD is characterized by a north–south precipitation dipole and a large positive surface air temperature anomaly. Positive feedback from transient eddy forcing reinforces the wavenumber-3-like propagation across extratropical regions, with ENSO playing a minor role compared to the IOD. This phenomenon is particularly evident in regions such as the North Pacific and North Atlantic, where wave energy propagation is intensified. Although SEAS5 replicates the NAO response, its magnitude is significantly weaker. The model struggles to simulate the delayed rainfall dipole response to the IOD accurately and shows structural discrepancies compared to reanalysis data.

KEYWORDS: Atmosphere-ocean interaction; ENSO; Teleconnections; Climate variability; North Atlantic Oscillation

1. Introduction

Several studies have investigated the teleconnections between El Niño–Southern Oscillation (ENSO) and the North Atlantic–European (NAE) region (Van Loon and Madden 1981; Rodó et al. 1997; Toniazzo and Scaife 2006; Brönnimann 2007; Herceg Bulić and Branković 2007; Bladé et al. 2008; García-Serrano et al. 2011; Trascasa-Castro et al. 2019; Mezzina et al. 2020, and others). The ENSO signals in the NAE are less intense and more challenging to demonstrate than those over the Pacific–North America (PNA) region (King et al. 2018a). Nevertheless, ENSO is considered the major mode of climate variability that influences the seasonal predictability in the extratropical regions including the North Atlantic (Domeisen et al. 2015; Herceg-Bulić et al. 2023; Geng et al. 2023b).

The teleconnection associated with a warm ENSO event starts in the central-eastern equatorial Pacific with sea surface temperature (SST) perturbations inducing positive rainfall and heating anomalies. The resulting upper-level divergence in the tropics (the opposite occurs for La Niña) serves as a source for the Rossby wave, which induces an extratropical wave train propagating northeastward and originating the signal in the PNA (Park et al. 2023). Subsequently, this teleconnection may extend its influence reaching the North Atlantic (Trenberth et al. 1998; Herceg Bulić and Branković 2007; Mezzina et al. 2020; Abid et al. 2021; Joshi et al. 2021).

ENSO anomalies modulate Euro-Atlantic circulation during late fall (November) (King et al. 2018b). Nevertheless, it is known that there is a transition of the Euro-Atlantic response from early to late winter through tropospheric and stratospheric pathways (Moron and Gouirand 2003; Garfinkel and Hartmann 2008; Scaife et al. 2017; Jiménez-Esteve and Domeisen 2018; Geng et al. 2023b). The canonical response to a positive ENSO event in the tropical Pacific yields a wave train inducing the negative phase of the North Atlantic Oscillation (NAO) in late winter (February–March). However, during early winter (December), the ENSO impact on the Euro-Atlantic response exhibits a wavenumber-3-like pattern leading to a positive NAO phase through the Indian Ocean (Abid et al. 2021; Joshi et al. 2021; Abid et al. 2023; Molteni and Brookshaw 2023; Zhang and Jiang 2023) and also through the Atlantic Ocean (Ayarzagüena et al. 2018; Hardiman et al. 2019).

ENSO influences the tropical Indian Ocean dynamics (Zhong et al. 2005; Cai et al. 2019), triggering, during boreal autumn, the development of an Indian Ocean dipole (IOD) event (e.g., Yang et al. 2015). The IOD can also manifest independently of ENSO (Saji et al. 1999; Ashok et al. 2003),

Supplemental information related to this paper is available at the Journals Online website: https://doi.org/10.1175/JCLI-D-23-0703.s1.

Corresponding author: Alessandro Raganato, araganato3@gatech.edu

DOI: 10.1175/JCLI-D-23-0703.1

and it has been shown to have global teleconnections (e.g., Saji and Yamagata 2003).

Abid et al. (2021) illustrated the role of the Indian Ocean precipitation in modulating the North Atlantic response to ENSO during boreal winter. Particularly, early winter ENSO triggers a precipitation dipole pattern over the Indian Ocean, inducing circulation perturbations within the South Asian subtropical jet (SAJET) region and modifying the SAJET itself. This alteration leads to shifts in rainfall patterns and increased predictability in the Southwest Asian winter monsoon region (Abid et al. 2020; Ma et al. 2022; Horan et al. 2024). These circulation perturbations in the SAJET region likely serve as the genesis of an upper-level Rossby wavenumber-3-like pattern propagating across Asia and the Pacific, ultimately impacting NAE regions in early winter and influencing the direct teleconnection from ENSO. However, in late winter, the atmospheric bridge between ENSO and the Indian Ocean precipitation weakens, and the NAE circulation is directly influenced by the direct ENSO teleconnection. Waves initiated within the SAJET region may exhibit distinct propagation characteristics compared to those directly initiated by ENSO due to the pronounced waveguiding effect (Branstator 2002) in the South Asian area. These waves, originating in the SAJET region, can traverse the North Pacific via the circumglobal waveguide (Bader and Latif 2005).

In the study conducted by Abid et al. (2023), the impact of western-central Indian Ocean (WCIO) precipitation anomalies on NAE circulation in early boreal winter was examined. Their findings suggest that while these anomalies are partly influenced by ENSO through an atmospheric bridge, their dominance stems from the autumn IOD. This hypothesis was tested by using the ECMWF SEAS5 prediction system by analyzing variations in WCIO precipitation prediction skills before and after removing the linear effects of ENSO and IOD, revealing a significant decline in prediction skills when the latter was removed. Following this approach, our present study focuses on isolating the contribution of IOD by linearly removing the influence of ENSO. Notably, we demonstrate that the response of Indian Ocean precipitation is strongly linked to IOD SST anomalies, and we further investigate the direct influence of these anomalies on extratropical atmospheric circulation.

The impact of the 2019/20 IOD event on the NAO has been explored by Hardiman et al. (2020), who also suggested a possible stratospheric teleconnection pathway. Additionally, other studies have shown that the Indian Ocean can counteract the direct boreal winter ENSO-induced Northern Annular Mode and PNA response (Fletcher and Kushner 2011; Fletcher and Cassou 2015). Seasonal forecasting systems can partly reproduce the response in the NAE regions to the Indian Ocean forcing, but with only about half of the observed magnitude, leading to a signal-to-noise paradox (Scaife and Smith 2018), but still show substantial predictability of the NAO and European temperature in early winter (Abid et al. 2023; Thornton et al. 2023; Hodson et al. 2023).

The importance of transient eddy wave flux in the ENSO teleconnections to the NAE region has been highlighted by Jiménez-Esteve and Domeisen (2018) and Scaife et al. (2019). Hardiman et al. (2022) suggested that models exhibiting weak transient eddy feedback also demonstrate limited ENSO teleconnections during the December–February period over the NAE regions, contributing to the signal-to-noise paradox. Moreover, numerous studies have emphasized the importance of transient eddy vorticity flux divergence for shaping the seasonal-mean extratropical atmospheric circulation anomalies, alongside the tropical forcing (Hoskins et al. 1983; Chang and Wallace 1987; Held et al. 1989; Ting and Held 1990; Hoerling and Ting 1994). These transients contribute to the seasonal-mean signals (Jin et al. 2006a,b; Kang et al. 2011; Abid et al. 2015), but it is imperative to acknowledge that they simultaneously introduce unpredictable noise (Rowell 1998; Kang and Kug 2002; Kang and Shukla 2006; Li and Lau 2012). There remains a lack of understanding of the specific impact of transient eddy feedback on the propagation of tropical-to-extratropical Rossby waves during early boreal winter (Swenson and Straus 2017).

It is well documented that models can reasonably well reproduce the ENSO response during late winter (Molteni and Brookshaw 2023; Williams et al. 2023). However, the early winter extratropical atmospheric circulation, mediated by the interbasin interactions, remains less understood. This knowledge gap holds significant implications for enhancing model accuracy in reproducing subseasonal to seasonal responses in the Euro-Atlantic regions.

Therefore, this study aims to investigate the independent IOD and combined IOD–ENSO delayed link with the Northern hemisphere extratropical circulation (particularly NAE) during the early phase of boreal winter. A pivotal aspect of our findings revolves around examining the specific association of IOD SST with transient eddy forcing that enhances the Rossby wave propagation over extratropical regions and amplifies the positive phase of the early winter NAO. This approach offers a novel perspective in understanding the mechanisms behind the wavenumber-3-like response triggered by the Indian Ocean precipitation anomalies identified by Abid et al. (2021).

Our study aims to explore how Indian Ocean October SST anomalies can directly induce a potentially predictable signal in both the December Indian Ocean precipitation and NAE circulation. Furthermore, this research seeks to evaluate the effectiveness of the ECMWF SEAS5 reforecast in capturing these specific teleconnections, conducting a detailed investigation to elucidate any potential reasons for weak teleconnections from the Indian Ocean. For this purpose, all findings will be compared against the fifth major global reanalysis produced by ECMWF (ERA5).

The datasets and model used are described in section 2. The methodology adopted is discussed in section 3. Results and discussion are presented in section 4. A summary and conclusions are presented in section 5.

2. Dataset and model

a. Reanalysis—ERA5

In the present study, the ERA5 dataset (Hersbach et al. 2020) is used for assessing IOD teleconnections.

ERA5 is based on the Integrated Forecasting System (IFS) Cy41r2 atmospheric model, which became operational in 2016. Moreover, ERA5 has benefited from a decade of enhancements

in model physics, core dynamics, and data assimilation techniques. This reanalysis dataset provides comprehensive coverage of Earth's atmosphere on an approximately 30-km grid, utilizing 137 hybrid sigma/pressure (model) levels from the surface up to an altitude of approximately 80 km. It also offers access to single-level data, featuring 2D parameters such as precipitation, top-of-atmosphere radiation, and vertical integrals spanning the entire atmospheric depth.

For our study, we consider the time frame spanning from 1981 to 2019, aligning with the period covered by the SEAS5 dataset (as elaborated in the subsequent section). Furthermore, the variables are examined on a regular grid of 1° longitude × 1° latitude. These variables include 200-hPa geopotential height, total precipitation, SST, surface air temperature (SAT), 100-hPa temperature, 100- and 200-hPa winds.

b. *The ECMWF seasonal hindcast dataset—SEAS5*

The ECMWF has maintained an operational real-time seasonal forecast system (SFS) since 1997. These forecasts involve computational models that calculate the evolution of the atmosphere, ocean, and land surface starting from an initial state based on observations of the Earth system. SEAS5, which replaced SEAS4 (Molteni et al. 2011) in 2017, represents the fifth generation of this system (Johnson et al. 2019). It incorporates upgraded versions of atmosphere and ocean models with enhanced resolutions. SEAS5 benefits from developments in its component models and initial condition generation. The IFS atmospheric model has seen improvements in representing tropical convection and has undergone an increase in horizontal resolution.

To verify the system and calibrate the forecast, SEAS5 uses a set of retrospective seasonal forecasts for past dates that can be compared to the historical record. The reforecasts used are initialized on 1 October and integrated for the next 6 months, spanning the years 1981–2019, and consist of 25 ensemble members. SEAS5 employs ECMWF's IFS atmosphere model cycle 43r1, characterized by a reduction in turbulent mixing under stable conditions, improving the representation of low-level jets. The IFS is coupled to the Nucleus for European Modelling of the Ocean (NEMO) v4.5 model. The atmospheric model uses a two-time-level semi-Lagrangian scheme for dynamics and has a 20-min time step (Johnson et al. 2019).

In SEAS5 reforecasts before 1 January 2017, the atmosphere is initialized using ERA-Interim data. For forecasts from 1 January 2017 onward, ECMWF operational analyses are used due to the unavailability of ERA-Interim reanalysis at the time of SEAS5 forecast initialization. Essentially, a hindcast approach is employed for the period 1981–2016, while a forecasting approach is adopted for 2017–19.

The model's variables are considered on a regular grid of 1° longitude × 1° latitude, similar to ERA5, and encompass the same parameters.

3. Methodology

a. *Indices and regression*

In this research, all data considered are linearly detrended. Furthermore, various indices are investigated to analyze the seasonal behavior of several phenomena. Here, an index is defined as either a variable averaged within a specific geographic region or as the difference between two regions (depicted on maps). The distribution of these indices' seasonal variations in the model is visually depicted using boxplots. In each case, the seasonal trends are constructed based on the regression field. The indices utilized are outlined in Table 1.

TABLE 1. Regions where indices are defined.

Name	Coordinates
Niño-3.4 index	5°S–5°N and 170°–120°W
IOD_{west} box	10°S–10°N and 50°–70°E
IOD_{east} box	10°S–0° and 90°–110°E
IOD index	$IOD_{west} - IOD_{east}$
NAO box, Azores	26°–40°N and 310°–360°E
NAO box, Iceland	50°–80°N and 310°–350°E
NAO index	NAO box, Azores − NAO box, Iceland
WCIO	10°S–10°N and 40°–90°E
IODPI	$IOD_{west} - IOD_{east}$

The estimated slope in simple linear regression can be expressed as the covariance between the normalized index and the field of interest (Molteni et al. 2015; Rashid et al. 2022):

$$\hat{\beta}(x, y) = \frac{1}{N}\sum_{i=1}^{N}\left[\frac{X(t_i)}{\sigma_X}\right] \times F(x, y, t_i), \tag{1}$$

where N is the number of years, $X(t)$ is an anomaly time series, σ_X is the standard deviation of the anomaly time series, and F is the anomaly map. The final result has the field's units.

The standard error associated with the slope regression coefficients (red bars in Fig. 9 and Figs. S6, S7, and S9 in the online supplemental material) is computed as

$$s_{\hat{\beta}} = \sqrt{\frac{1}{N-1}\frac{\sum_{i=1}^{N}\hat{\varepsilon}_i^2}{\sum_{i=1}^{N}\left[\frac{X(t_i)}{\sigma_X}\right]^2}}, \tag{2}$$

where ε_i denotes the residuals expressed as

$$\hat{\varepsilon}_i = F_i - \hat{\beta}\frac{X(t_i)}{\sigma_X}. \tag{3}$$

The partial regression method is employed to disentangle the links of IOD and/or ENSO atmospheric forcings on NAE anomalies (Kucharski et al. 2009; Abid et al. 2021). The method involves the following equation:

$$X_{res}(t) = X(t) - b \times X_{rem}(t), \tag{4}$$

where b represents the regression coefficient between the anomaly index to be removed (X_{rem}) and the considered

anomaly index (X). The resulting X_{res} is a residual time series that is uncorrelated with X_{rem}.

For instance, to examine a residual IOD SST time series with the influence of ENSO removed, the following equation is applied:

$$\text{IOD}_{\text{res}}(t) = \text{IOD}(t) - b \times \text{Nino-3.4}(t). \tag{5}$$

In this context, the Niño-3.4 and IOD terms correspond to the SST anomalies indices described in Table 1. In all cases examined, the SST time series are calculated fixed in October since this is when the Indian Ocean dipole typically attains its maximum activity. Furthermore, regressions are performed separately for individual ensemble members and then averaged when considering the SEAS5 dataset. To determine statistical significance in each regression map, we implemented a false discovery rate (FDR) method for multiple hypothesis testing as described by Wilks (2016).

b. Wave activity flux

To analyze the source and direction of energy propagation, wave activity flux (WAF) formulated by Takaya and Nakamura (1997, 2001) is applied. The wave activity in the stationary case is defined as

$$\mathbf{W} = \frac{p\cos\varphi}{2|\mathbf{U}|}\begin{Bmatrix} \dfrac{U}{a^2\cos^2\varphi}\left[\left(\dfrac{\partial\psi'}{\partial\lambda}\right)^2 - \psi'\dfrac{\partial^2\psi'}{\partial\lambda^2}\right] + \dfrac{V}{a^2\cos\varphi}\left(\dfrac{\partial\psi'}{\partial\lambda}\dfrac{\partial\psi'}{\partial\varphi} - \psi'\dfrac{\partial^2\psi'}{\partial\lambda\partial\varphi}\right) \\ \dfrac{U}{a^2\cos\varphi}\left(\dfrac{\partial\psi'}{\partial\lambda}\dfrac{\partial\psi'}{\partial\varphi} - \psi'\dfrac{\partial^2\psi'}{\partial\lambda\partial\varphi}\right) + \dfrac{V}{a^2}\left[\left(\dfrac{\partial\psi'}{\partial\varphi}\right)^2 - \psi'\dfrac{\partial^2\psi'}{\partial\varphi^2}\right] \\ \dfrac{f_0^2}{N^2}\left[\dfrac{U}{a\cos\varphi}\left(\dfrac{\partial\psi'}{\partial\lambda}\dfrac{\partial\psi'}{\partial z} - \psi'\dfrac{\partial^2\psi'}{\partial\lambda\partial z}\right) + \dfrac{V}{a}\left(\dfrac{\partial\psi'}{\partial\varphi}\dfrac{\partial\psi'}{\partial z} - \psi'\dfrac{\partial^2\psi'}{\partial\varphi\partial z}\right)\right] \end{Bmatrix}, \tag{6}$$

where p is the pressure normalized by 1000 hPa, f_0 is the Coriolis parameter at 45°N, a is Earth's radius, N is the Brunt–Väisälä frequency, ϕ is the latitude, λ is the longitude, U and V represent the basic states derived from the monthly mean climatology, and ψ' represents the perturbed streamfunction. In the present study, ψ' is derived from the 200-hPa geopotential height anomaly regressed onto the standardized total and residual IOD index.

c. Transient eddy forcing and time response

Transient eddies are identified by applying a 2–10-day bandpass filter to the time series of variables using a fast Fourier transform (FFT)-based method. In the case of SEAS5, transient eddy calculations are performed individually for each ensemble member.

The transient eddy forcing component is intended as the 200-hPa geopotential height tendency, specifically arising from the anomalous transient vorticity flux divergence. The formulation of this forcing term, as defined in prior studies by Kang et al. (2011) and Abid et al. (2015), is expressed as follows:

$$\left(\frac{\partial\overline{\phi}^a}{\partial t}\right)_{\text{tr}} = -\frac{f}{g}\nabla^{-2}\left[\nabla\cdot\left(\overline{\mathbf{V}'\zeta'}^a\right)\right]. \tag{7}$$

In this equation, f represents the Coriolis parameter, g is the gravity, ζ denotes the vorticity, $\mathbf{V}$ signifies the wind vector, and ϕ corresponds to the 200-hPa geopotential height. The terms $\mathbf{V}'$ and ζ' are obtained by applying a 2–10-day bandpass filter to the time scale of the wind components using an FFT-based method. The overbars denote the seasonal-mean, and the superscripts a signify the seasonal-mean anomaly from the climatology.

The intensity of transient forcing's impact on seasonal-mean circulation can be quantified using the time-response parameter $J(t)$ as defined by Kang et al. (2011) and Abid et al. (2015):

$$J(t) = \frac{\int\int\left[\overline{\phi_{\text{reg}}}^a(x,y)\right]^2 dxdy}{\int\int\overline{\phi_{\text{reg}}}^a(x,y)\times\left(\dfrac{\partial\overline{\phi}^a}{\partial t}\right)_{\text{tr}}(x,y)\,dxdy}, \tag{8}$$

where $\overline{\phi_{\text{reg}}}^a(x,y)$ represents the 200-hPa geopotential height anomalies regressed onto the normalized total and residual IOD SST index over the domain spanning 20°–75°N and 120°W–180°.

d. Heat fluxes

The meridional eddy heat flux at 100 hPa is used as a measure for the upward propagation of planetary waves (Hinssen and Ambaum 2010). This investigation is based on the following equation:

$$\text{HF} = v^*\cdot T^*, \tag{9}$$

where v^* and T^* are the deviations from the zonal mean of the 100-hPa meridional wind and temperature, respectively.

4. Results and discussion

a. Tropical-to-extratropical teleconnections during boreal winter

The February 200-hPa geopotential height regressions onto the Niño-3.4 SST anomalies index for the period 1981–2019

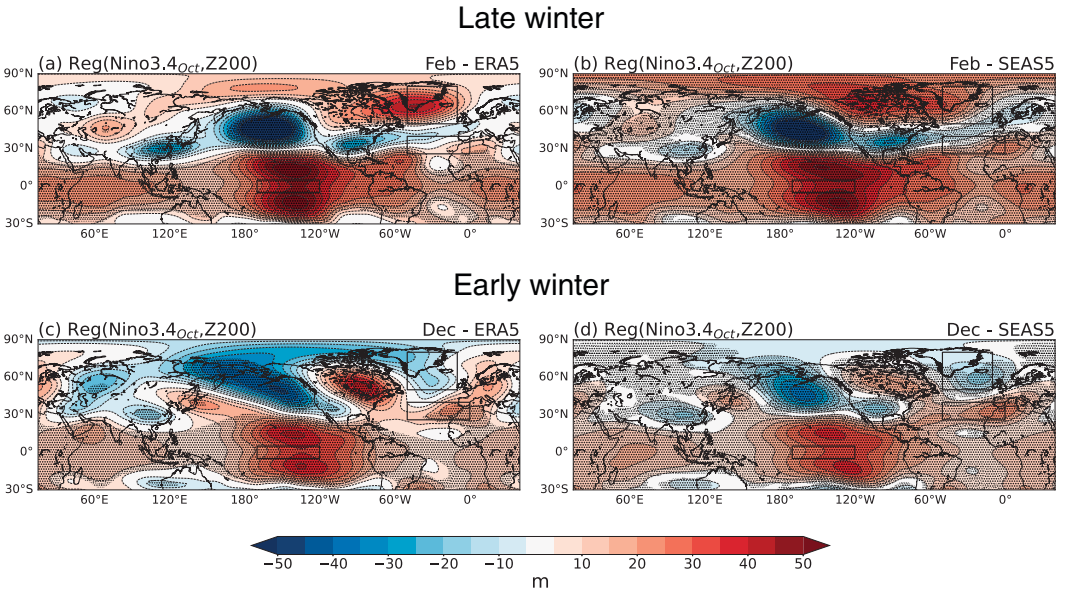

FIG. 1. (a) Regression map of February reanalysis (ERA5) 200-hPa geopotential height anomalies (m) onto the corresponding Niño-3.4 SST anomalies index (5°S–5°N and 170°–120°W) fixed in October for the period 1981–2019. (b) As in (a), but with the average over the 25 ensemble members of the ECMWF reforecast dataset (SEAS5). (c) As in (a), but for the early winter (December) case in ERA5. (d) As in (c), but with the average over the 25 ensemble members of the ECMWF reforecast dataset (SEAS5). Stippling denotes statistical significance calculated using an FDR method for multiple hypothesis testing. Boxes over the North Atlantic denote the NAO index defined as the difference between the regions highlighting the Azores (26°–40°N and 310°–360°E) and Iceland (50°–80°N and 310°–350°E).

are presented in Fig. 1a for reanalysis and in Fig. 1b for SEAS5. In both the cases, a notable NAO negative phase is found as an extension of the Rossby wave originating from the central-eastern equatorial Pacific and propagating across North America and the Euro-Atlantic regions. The reanalysis data depict a slightly clearer North Atlantic response, as the model tends to shift positive geopotential height anomalies over North America. Nevertheless, SEAS5 exhibits a generally commendable performance in simulating these teleconnections during late boreal winter. Additionally, the December 200-hPa geopotential height regressions onto Niño-3.4 SST anomalies are presented in Figs. 1c and 1d for both ERA5 and SEAS5. During early winter, the upper-level Rossby wave propagating from the central-eastern equatorial Pacific affects the PNA regions and leads to a positive NAO phase. Moreover, during early winter, the contribution of a Rossby wave coming from the Indian Ocean becomes more relevant than in late winter (Abid et al. 2021, 2023). This feature is highlighted by the extension of negative geopotential height anomalies over Asia in Fig. 1c. Notably, SEAS5 effectively reproduces these teleconnections in December as well (Fig. 1d).

However, the scenario undergoes significant changes in Fig. 2, where the early winter 200-hPa geopotential height regressions with residual (IOD with ENSO removed) and total IOD SST anomalies, for the period 1981–2019, are depicted again for reanalysis and model. Arrows illustrate the WAF related to stationary Rossby waves, hereafter referred to as Rossby WAF (RWAF). In Fig. 2a, ERA5 shows a wavenumber-3-like response originating from the Indian Ocean and propagating through the extratropical regions, linearly associated with the early winter positive NAO pattern. This wave response is not only related to the specific negative geopotential height anomaly previously studied by Abid et al. (2021) but also more comprehensively linked to the presence of a positive-to-negative geopotential height dipole extending across East Africa and South Asia (Abid et al. 2020). Specifically, the positive anomaly is associated with the convective processes generated by the warm pole of the IOD. Furthermore, it is noteworthy that the negative anomalies in the North Pacific and North Atlantic are intense and statistically significant (see Fig. S1), indicating a strengthening of the wave train in these areas, as confirmed by the RWAF. The underlying characteristics of these anomalies will be subject to further investigation in section 4c. In SEAS5, wave trains are visible, but with much smaller amplitude. Moreover, the positive anomaly over Asia has now shifted eastward over Japan compared to the reanalysis. The positive NAO response is reproduced with much-reduced amplitude (Fig. 2b compared to Fig. 2a).

In the regressions onto the total IOD SST index in ERA5 (Fig. 2c), the positive anomalies over the central Pacific begin to play a more significant role in the Rossby wave propagation, as also indicated by the increased RWAF in those regions. This leads to northeastward propagation through the PNA and North Atlantic regions. Furthermore, in the total IOD regression case, the negative geopotential height anomaly over the North Pacific and the positive anomaly over North America are intensified. Additionally, a new negative anomaly arises in Southeast Asia, where there is now a

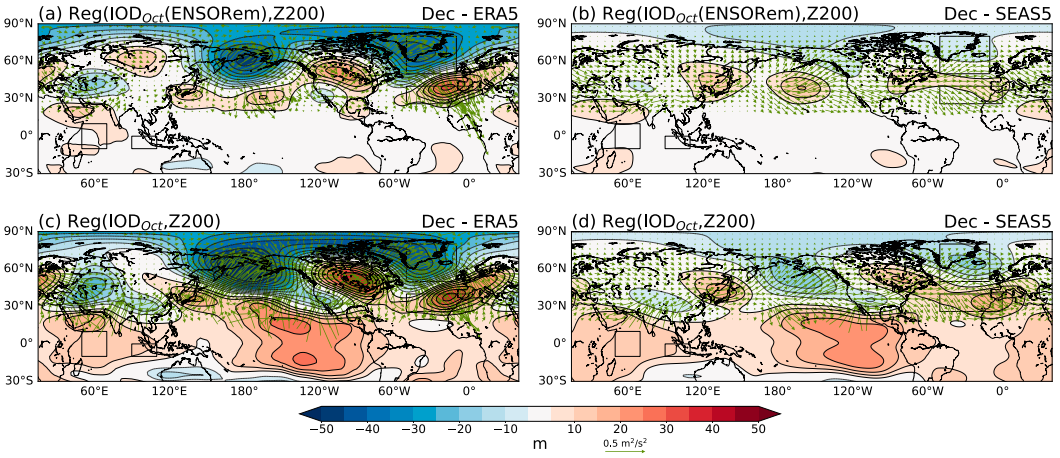

FIG. 2. (a) Regression map of December reanalysis (ERA5) 200-hPa geopotential height anomalies (m) onto the corresponding IOD_{res} SST anomalies index (east box: 10°S–0° and 90°–110°E; west box: 10°S–10°N and 50°–70°E) fixed in October for the period 1981–2019. (b) As in (a), but for the average over the 25 ensemble members of the ECMWF reforecast dataset (SEAS5). (c) Regression map of December reanalysis (ERA5) 200-hPa geopotential height anomalies (m) onto the corresponding total IOD SST anomalies index fixed in October for the period 1981–2019. (d) As in (c), but for the average over the 25 ensemble members of the ECMWF reforecast dataset (SEAS5). Arrows denote RWAF. Boxes over the North Atlantic denote the NAO index defined as the difference between the regions highlighting the Azores (26°–40°N and 310°–360°E) and Iceland (50°–80°N and 310°–350°E).

gradient aiding the initiation of the wavenumber-3-like response from the Indian Ocean (Geng et al. 2023a). SEAS5's results shown in Fig. 2d present a weaker signal almost everywhere compared to ERA5, as well as the IOD_{res} case. However, the model reproduces similar changes to reanalysis, extending the negative geopotential height anomaly over Southeast Asia and enhancing the positive anomaly in the North Pacific. In general, the RWAF intensity is weaker everywhere in the model compared to the reanalysis. Furthermore, the differences between total and residual regression in SEAS5 seem to bring small changes in RWAF compared to the changes happening in ERA5 over key regions such as the North Pacific and North Atlantic. Refer to Fig. S2 for additional information on the January regressions onto the IOD, IOD_{res}, and Niño-3.4 SST index anomalies. It is a valuable resource for further exploration and analysis.

To support the validity of using a partial regression method to isolate the IOD link with the atmospheric circulation from ENSO, we conduct a composite analysis considering neutral ENSO years defined by the October |Niño-3.4 SST index| < 1 K and the years with an October IOD SST anomaly intensity greater than 0.4 K (see bold years in Table 2). Specifically, we consider half of the difference in the December 200-hPa geopotential height between positive and negative IOD phases during such years. Results depicted in Fig. 3 show a clear positive NAO phase, indicating a linear relationship between IOD and NAO. Remarkably, the positive anomaly over the central Pacific associated with the ENSO component is not fully removed by the composite analysis. However, further reducing the threshold below 1 K in defining neutral ENSO years would result in an insufficient sample size for meaningful analysis.

For a more precise assessment of the model's ability to reproduce the atmospheric circulation over the NAE regions, a focus on the NAO representation is crucial. The NAO index described in Table 1 (Abid et al. 2023) is calculated from the 200-hPa geopotential height regressions onto total and residual IOD and Niño-3.4 SST anomalies. All the results are presented in Fig. 4. The January–March monthly results are also presented for the sake of completeness, even though this period is of limited interest in this study due to the marginal influence of the IOD on tropical-to-extratropical teleconnections when ENSO is dominant.

The robust relationship between the IOD and NAO becomes apparent when examining the correlation coefficients between their respective time series as depicted in the correlation matrix of Fig. S3. Specifically, a correlation coefficient of 0.43 is observed for the IOD_{res} case and 0.49 for the total IOD, both significant at the 95% confidence level in ERA5.

TABLE 2. Neutral ENSO years considered for composite analysis. The (+) indicates years with positive October IOD SST anomalies, while (−) indicates years with negative October IOD SST anomalies. The bold font denotes years with $|IOD_{oct}$ SST anomalies$| > 0.4$ K.

Years with |Niño-3.4 October SST anomalies| < 1 K
1981$^-$, 1983$^-$, **1984$^-$**, **1985$^-$**, 1986$^+$, 1989$^-$, **1990$^-$**, **1991$^+$**, **1992$^-$**, 1993$^-$, **1994$^+$**, **1996$^-$**, 2000$^-$, **2001$^-$**, 2003$^-$, 2004$^+$, **2005$^-$**, **2006$^+$**, 2008$^-$, 2009$^-$, **2012$^+$**, 2013$^-$, 2014$^+$, **2016$^-$**, 2017$^-$, 2018$^+$, **2019$^+$**

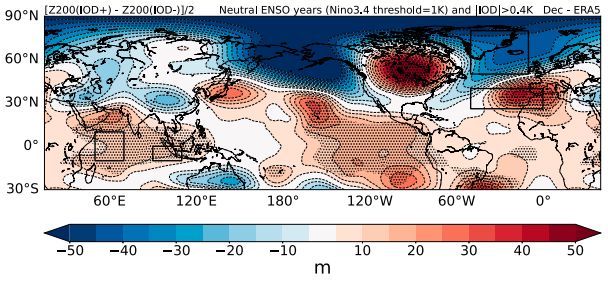

FIG. 3. Half of the difference in the December 200-hPa geopotential height during neutral ENSO years (threshold of 1 K) between positive and negative |IOD| > 0.4 K years in ERA5. Stippling denotes statistical significance calculated using an FDR method for multiple hypothesis testing.

In Fig. 4a, the regression onto the SST anomalies associated with the IOD_{res} fixed in October is considered. Examining the reanalysis, we find that a positive IOD, peaking in October, is associated with a delayed positive NAO signal in the extratropics during early winter (see also Fig. 2a). Further confirmation of the IOD's dominance during this part of the season in ERA5 is seen in Fig. 4b, where the regression onto the residual Niño-3.4 SST anomalies is considered. Here, the residual anomalies represent the direct ENSO component with the effects of the IOD removed. Thus, for the reanalysis, in December, the NAO index associated with the residual ENSO is negative, which is opposite to that of the IOD_{res} case. Therefore, the total Niño-3.4 case (Fig. 4d), which presents a positive NAO index in December, indicates that the tropical-to-extratropical atmospheric bridge coming from the Indian Ocean dominates over the one from central-eastern equatorial Pacific. Similar considerations can be made when comparing the small difference between IOD_{res} and the total IOD in ERA5 during early winter (Fig. 4c). It is also interesting to note that the positive NAO associated with the residual IOD becomes weaker starting from January as the direct ENSO contribution becomes more prominent during late winter (February) when a negative NAO phase arises (see Fig. 1 and descending trends in Figs. 4a,c).

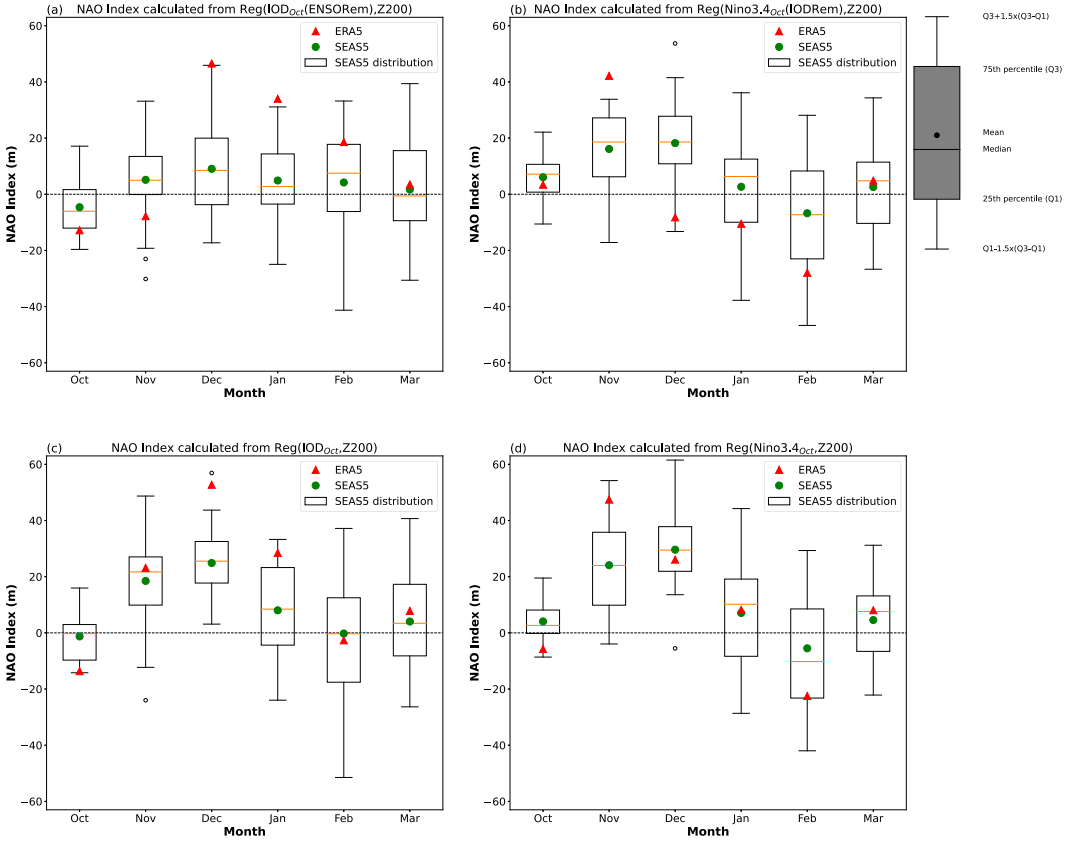

FIG. 4. (a) NAO index (m) defined as the difference between the regions highlighting the Azores (26°–40°N and 310°–360°E) and Iceland (50°–80°N and 310°–350°E), for the 25 ensemble members of the ECMWF reforecast (SEAS5) and reanalysis (ERA5) dataset, as a function of winter's months in the case of the 200-hPa geopotential height regression onto the corresponding residual IOD SST anomalies index fixed in October for the period 1981–2019. Empty dots are outliers; red triangles stand for the reanalysis climatology. (b) As in (a), but for the regression onto the residual Niño-3.4 SST anomalies index fixed in October. (c) As in (a), but for the regression onto the total IOD SST anomalies index fixed in October. (d) As in (a), but for the regression onto the total Niño-3.4 SST anomalies index fixed in October.

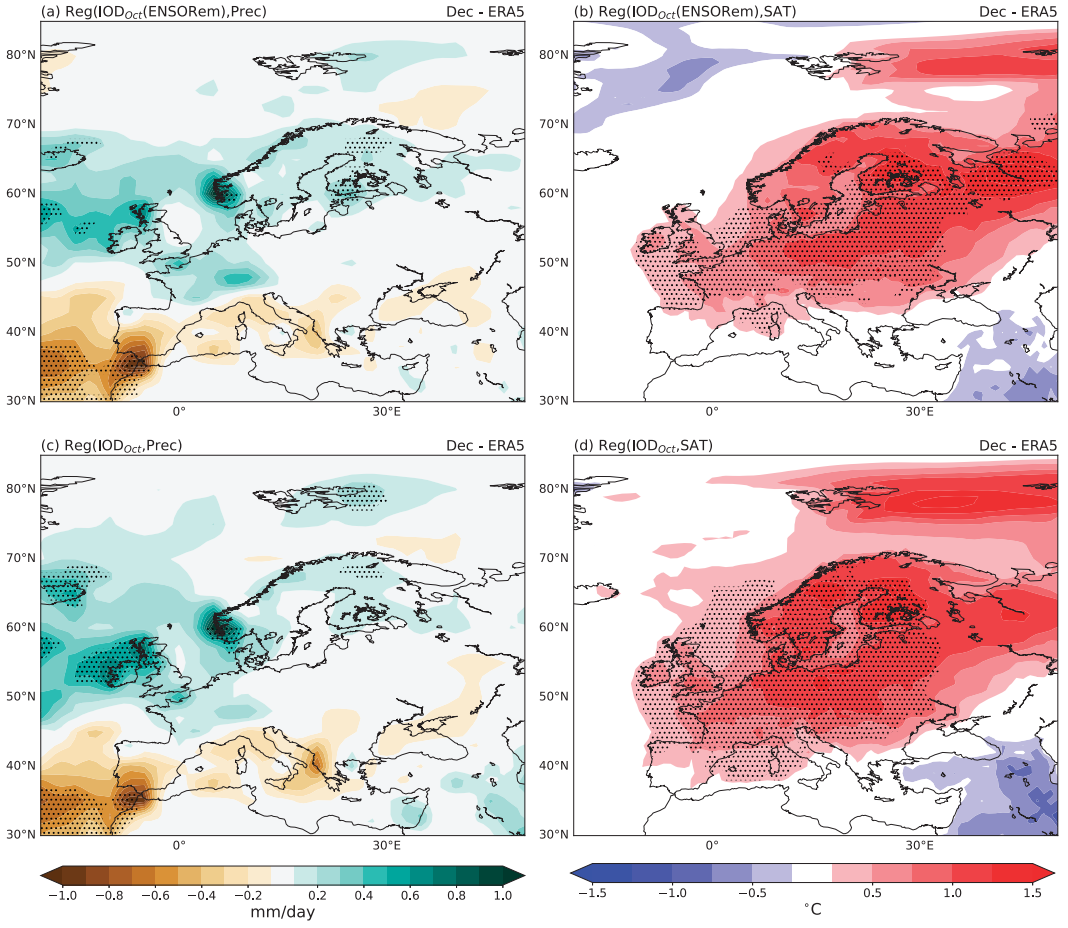

FIG. 5. (a) Regression map of December reanalysis (ERA5) total precipitation anomalies (mm day^{-1}) onto the corresponding IOD$_{res}$ SST anomalies index (east box: 10°S–0° and 90°–110°E; west box: 10°S–10°N and 50°–70°E) fixed in October for the period 1981–2019. (b) Regression map of December reanalysis (ERA5) SAT anomalies (°C) onto the corresponding IOD$_{res}$ SST anomalies index fixed in October for the period 1981–2019. (c) As in (a), but considering the regression onto the total IOD SST anomalies index. (d) As in (c), but considering the SAT anomalies (°C). Stippling denotes statistical significance calculated using an FDR method for multiple hypothesis testing.

Regarding SEAS5's results, we find almost the same correlation coefficient of 0.27 in the NAO–Niño-3.4 pair compared to the one from the reanalysis of 0.24 (see Fig. S3). However, the model seems to underestimate the relationships between NAO and IOD/IOD$_{res,}$ presenting a halved correlation coefficient compared to ERA5 in these two cases. The lower intensity of the NAO index is associated with the weaker tropical-to-extratropical atmospheric bridge during early winter (Fig. 2a). As shown in Fig. 4a, the green dot in December has a lower magnitude compared to reanalysis. Furthermore, while SEAS5 captures the correct NAO phase, the boxplots and whiskers indicate that the ensemble distributions fail to replicate the ERA5 magnitude in December and January. For the total IOD case (Fig. 4c), improvements are observed in January, where the model distribution aligns with reanalysis. This improvement is likely attributed to the increasing influence of ENSO on these teleconnections in mid-to-late winter. However, the weaker NAO delayed response to IOD during early winter persists for the total regression as well, except for one outlier, slightly exceeding ERA5. Furthermore, in ERA5, residual ENSO shows a negative NAO from December to February, whereas the total ENSO contribution highlights the influence of the IOD in December and January, associated with an NAO switch. SEAS5 consistently portrays a positive NAO phase in December and January for both the regression onto total and residual Niño-3.4. Moreover, the early winter NAO positive phase for the residual Niño-3.4 case (December, green dot in Fig. 4b) is slightly greater than the one of IOD$_{res}$ (December, green dot in Fig. 4a). Therefore, the correct early winter result shown by the model for the total Niño-3.4 (Fig. 4d) is influenced by the Pacific Ocean forcing, in contrast to reanalysis, where the positive December NAO phase is primarily associated with the tropical-to-extratropical atmospheric bridge with the Indian Ocean.

b. The European surface climate response

The relationships between the IOD and rainfall and SAT anomalies based on ERA5 data over European regions during

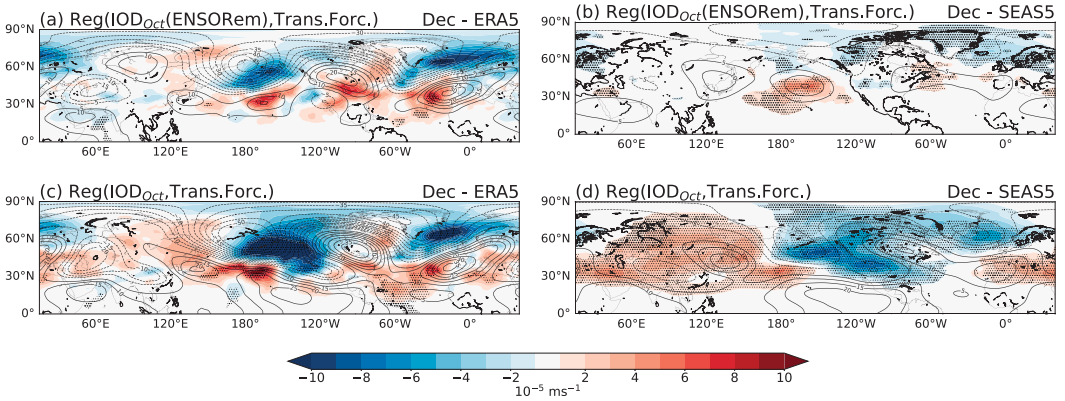

FIG. 6. (a) Regression map of December reanalysis (ERA5) transient eddy forcing anomalies (m s^{-1}) onto the corresponding IOD$_{res}$ SST anomalies index (east box: 10°S–0° and 90°–110°E; west box: 10°S–10°N and 50°–70°E) fixed in October for the period 1981–2019. (b) As in (a), but with the average over the 25 ensemble members of the ECMWF reforecast dataset (SEAS5). (c) Regression map of December reanalysis (ERA5) transient eddy forcing anomalies (m s^{-1}) onto the corresponding total IOD SST anomalies index fixed in October for the period 1981–2019. (d) As in (c), but with the average over the 25 ensemble members of the ECMWF reforecast dataset (SEAS5). Stippling denotes statistical significance calculated using an FDR method for multiple hypothesis testing. Contours (5-m interval with dashed lines indicating negative values) represent the regressions of December 200-hPa geopotential height onto the corresponding indices for each case.

early winter are presented in Fig. 5. Figure 5a shows the total precipitation regression onto the residual IOD SST index. Notably, the classical fingerprint of a positive NAO is discernible, meaning that a positive IOD phase is associated with increased precipitation in northern Europe and diminished rainfall in the southern part of the continent. These alterations manifest prominently over regions like southern Spain and Norway. Meanwhile, the regression onto the total IOD SST index (Fig. 5c) does not reveal significant differences from the previous case, barring a pronounced positive anomaly over northern United Kingdom and Ireland, suggesting that the ENSO component does not play a crucial role in shaping the rainfall pattern during this part of the season. Similar analyses considering the SAT regressions are depicted in Figs. 5b and 5d. The positive NAO phase associated with the IOD leads to an extensive surface warm anomaly spanning the entire central-northern European region. Furthermore, a comparison between the regression onto the residual and total IOD SST indices does not reveal substantial changes in the surface temperature pattern either. Results for SEAS5 are considerably weaker (see Fig. S4) both in terms of total precipitation and SAT. This weakened early winter signal in the model is likely attributed to the reduced NAO response (see discussion and Fig. S5).

c. *Transient eddy forcing*

The transient activity induces the forcing that impacts the seasonal-mean circulation anomalies (Hardiman et al. 2022). It is worth investigating whether similar dynamics come into play within the NAE regions in response to tropical IOD forcing.

To investigate the early winter IOD connection with the transient eddy forcing anomalies (see section 3c), its December regressions onto the residual and total IOD SST indices fixed in October are presented in Fig. 6. Both reanalysis and model results exhibit great similarities, within the North Atlantic and North Pacific regions, between the transient forcing and the 200-hPa geopotential height anomalies (Fig. 2 and contours in Fig. 6).

Regarding the IOD$_{res}$ case for ERA5, the strong geopotential height negative anomalies observed over the North Pacific and the North Atlantic, discussed in section 4a, are substantially reinforced by positive feedback from transient eddy forcing. Specifically, the blue anomalies over the NAE regions and the North Pacific in Figs. 6a and 6c mirror the patterns observed with the contours. This explains why, during early winter, ERA5 exhibits a wave train that is intensified in those parts of the extratropics. Notably, when incorporating the ENSO component in Fig. 6c, we find a more robust forcing anomaly response in the North Pacific sector. This, in turn, translates into a more pronounced Rossby wave emanating from the central-eastern equatorial Pacific, as observed in Fig. 2c, in comparison to the residual case.

Figures 6b and 6d present the same analyses for SEAS5. In both the cases, whether considering the residual or total IOD indices, the transient forcing in the model is notably weaker than in reanalysis data. In the IOD$_{res}$ case, the model does capture the location of positive anomalies over the North Pacific, probably facilitating the propagation of extratropical Rossby waves depicted in Fig. 2b. Furthermore, the negative anomaly observed over the North Atlantic enhances the positive NAO signal evident in the 200-hPa geopotential height contours. When adding the ENSO component (Fig. 6d), the negative anomalies intensify, not only over North America and the North Pacific but also over the North Atlantic, further enhancing the positive NAO phase and the Rossby wave train (Fig. 2d). Additionally, extensive positive anomalies dominate the Asian region, exhibiting consistency with reanalysis.

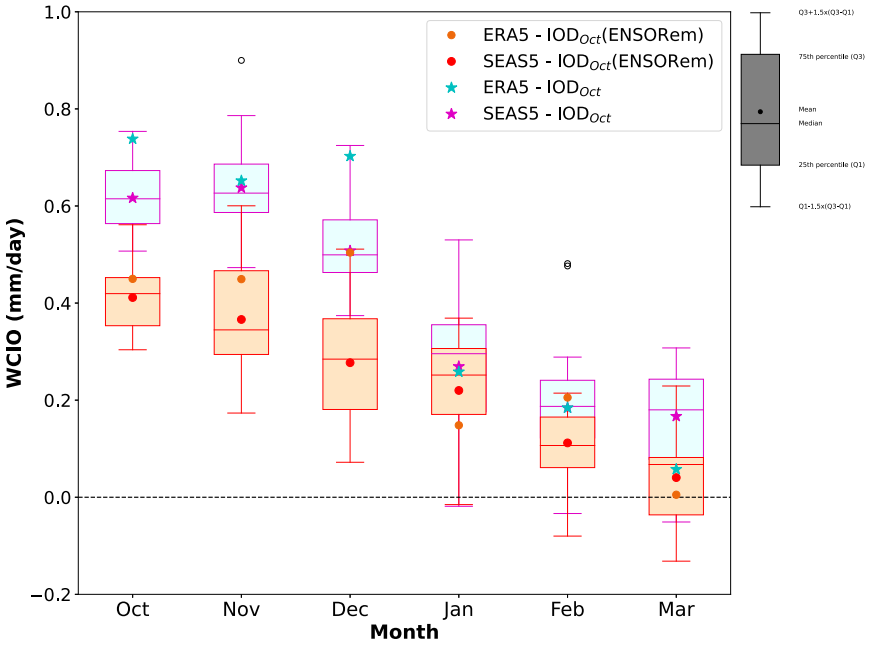

FIG. 7. WCIO (mm day^{-1}) defined as the average inside 10°S–10°N and 40°–90°E for the 25 ensemble members of the ECMWF reforecast (SEAS5) and reanalysis (ERA5) dataset as a function of winter's months in the case of the precipitation regression onto the corresponding total and residual IOD SST anomalies index fixed in October for the period 1981–2019. Orange (blue) boxes refer to the SEAS5 ensemble members' distribution in the residual (total) regression case; orange dots and light blue stars stand for the reanalysis (ERA5) climatology for the IOD$_{res}$ and IOD regression, respectively.

To quantify the intensity of transient forcing's impact on seasonal-mean circulation, the time response is used (see section 3c). For reanalysis, the $J(t)$ parameter values are 8.4 and 8.1 days for the December transient forcing regressions onto the residual and total IOD SST indices, respectively. The model yields $J(t)$ values of 7.9 and 9.4 days for residual and total IOD regressions, respectively, indicating strong feedback between transient forcing and geopotential height. However, in SEAS5, the initial response may be so weak that the transient eddy feedback is not enough to strengthen the 200-hPa geopotential height response sufficiently to be close to ERA5. Furthermore, the time responses related to the December residual and total Niño-3.4 regressions are 11.2 and 8 days, respectively, for reanalysis, while for SEAS5, it is found to be 10 and 11.5 days. The weaker transient response in ENSO compared to IOD aligns well with Hardiman et al. (2022), who demonstrated that models such as SEAS5, which exhibit a deficit in simulating these dynamics, also show weaker skills in capturing the extratropical atmospheric circulation response to ENSO.

d. The Indian Ocean precipitation response

Several factors may contribute to the differences observed between Figs. 2a and 2b. One explanation could be the model's difficulty in directly simulating the rainfall dipole pattern over the Indian Ocean.

To further investigate this aspect, the regressions of total precipitation onto the total and residual IOD SST anomalies index fixed in October are considered. The WCIO index (mm day^{-1}, see the red box in Fig. 8) is then calculated considering the definition in Table 1 (Abid et al. 2023). Results are presented in Fig. 7 where both model and reanalysis are reported for the two different cases of WCIO calculated with the regression onto the total (blue and purple stars) and residual (orange and red dots) IOD SST anomalies. The boxplots focus on SEAS5's 25 ensemble members distribution. Error bars for the reanalysis are shown in Fig. S6.

Concerning ERA5, in each scenario depicted in Fig. 7, the WCIO's positive phase dominates the entire trend. Additionally, it diminishes as winter progresses with ENSO taking control of tropical dynamics and becoming the dominant mode of variability for tropical-to-extratropical teleconnections. The IOD, whose SST anomalies are already weak in December, demonstrates a delayed link with the precipitation pattern, indicating that the strong dipole in October and November is associated with the Indian Ocean's rainfall in December when the WCIO is still considerably positive. Then, a significant drop in the WCIO index between December and January, particularly evident in the total IOD case, highlights the weakened Indian Ocean precipitation response in mid-to-late winter. In December, WCIO associated with the residual IOD represents 71% of the total IOD contribution, while the residual ENSO constitutes only 16% of the total Niño-3.4 (see Fig. S6).

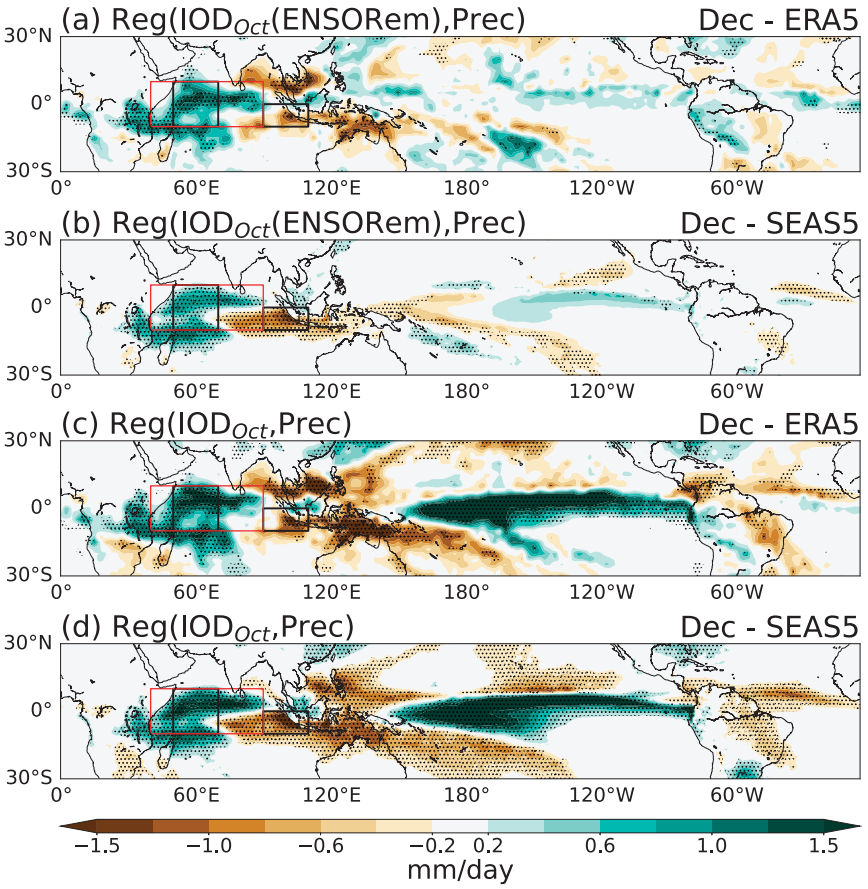

FIG. 8. (a) Regression map of December reanalysis (ERA5) total precipitation anomalies (mm day^{-1}) onto the corresponding residual IOD SST anomalies index (east box: 10°S–0° and 90°–110°E; west box: 10°S–10°N and 50°–70°E) fixed in October for the period 1981–2019. (b) As in (a), but for the average over the 25 ensemble members of the ECMWF reforecast dataset (SEAS5). (c) Regression map of December reanalysis (ERA5) total precipitation anomalies (mm day^{-1}) onto the corresponding total IOD SST anomalies index fixed in October for the period 1981–2019. (d) As in (c), but for the average over the 25 ensemble members of the ECMWF reforecast dataset (SEAS5). Stippling denotes statistical significance calculated using an FDR method for multiple hypothesis testing. The red box represents the WCIO index (10°S–10°N and 40°–90°E).

This suggests that the early winter precipitation response is predominantly associated with the October IOD SST anomalies.

This aspect is also suggested when considering the IOD precipitation index (IODPI) defined using the same boxes as the IOD index (see Table 1). Indeed, the results in Fig. S8 depict an IODPI still considerably greater than 1 mm day^{-1} in December.

The SEAS5's WCIO response in Fig. 7 suggests that the model underestimates the December total precipitation response in both total and residual IOD cases. In this case, the model's index value for the residual case is only 52% of that of ERA5 (72% for the total regression case).

To identify significant issues in the total precipitation pattern, complete maps of December total precipitation regressions with residual and total IOD SST indices fixed in October are presented in Figs. 8a and 8c for ERA5 and Figs. 8b and 8d for the SEAS5's ensemble mean.

In all cases, ERA5 exhibits noisier patterns compared to SEAS5, as expected due to the averaging of the 25 ensemble members in the model results. This difference is particularly noticeable over the Indian and Pacific Oceans in the total IOD regressions (Figs. 8c,d). Analyses with the residual IOD SST index reveal a more intense western component of the rainfall dipole in the reanalysis than in the model, along with a dry region over Thailand that the model fails to capture entirely. Even when considering the ENSO component (Fig. 8d), the model reproduces the increased dry region over the western Pacific but still misses the pattern over the eastern Indian Ocean. Moreover, SEAS5 exhibits a more pronounced eastern rainfall dipole component extended over the central Indian Ocean, compared to the reanalysis (Mayer et al. 2023). As a result, the model introduces a substantial latitudinal gradient to the precipitation dipole pattern (Molteni et al. 2020), which is

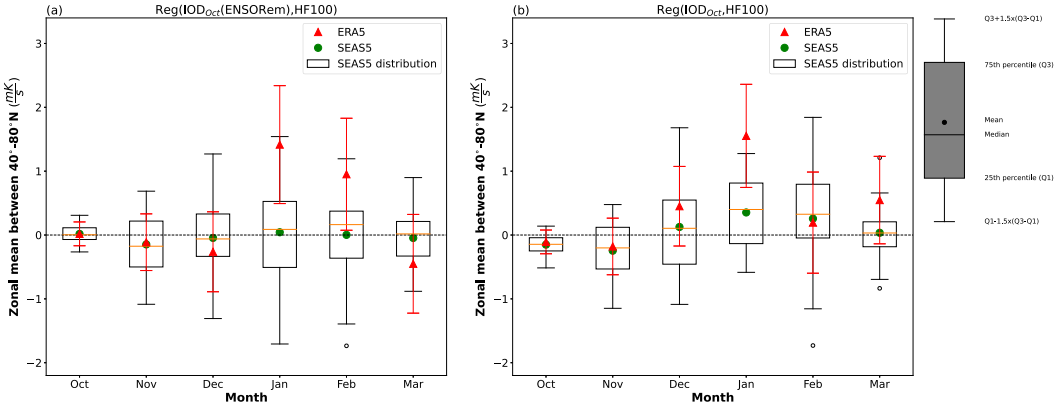

FIG. 9. (a) Regression coefficients (m K s^{-1}) from the 100-hPa heat fluxes regression onto the IOD_{res} SST anomalies index (east box: 10°S–0° and 90°–110°E; west box: 10°S–10°N and 50°–70°E) fixed in October for the period 1981–2019 averaged zonally between 40° and 80°N latitudes as a function of boreal winter's months. Empty dots are outliers; red triangles stand for the reanalysis (ERA5) climatology; red error bars illustrate the standard error associated with the regression coefficients in ERA5. (b) As in (a), but for the regression onto the total IOD SST anomalies index fixed in October.

further intensified when considering the influence of ENSO, as observed in the total IOD regressions (Zhao et al. 2023).

e. *Stratospheric pathway*

Another plausible explanation for the differences observed in Fig. 2b compared to Fig. 2a could be related to difficulties in reproducing the wave activity flux into the polar stratosphere. To investigate this aspect, the meridional eddy heat flux at 100 hPa is considered as defined in section 3d. Specifically, it is well documented that a positive NAO phase is strengthened by stratospheric cooling anomalies (Shaw et al. 2014).

To elucidate the influence of the IOD on the vertical propagation of planetary waves impacting the stratosphere, the 100-hPa HF [Eq. (9)] regression onto the residual and total IOD SST index over the period 1981–2019 is employed as done in earlier sections. Subsequently, the results from these regressions are zonally averaged within the latitudinal range of 40°–80°N to capture the wave activity flux into the polar stratosphere (Hinssen and Ambaum 2010). The resulting values (m K s^{-1}) for the period spanning from October to March are displayed in Fig. 9.

Negative values in the data indicate stratospheric cooling, which translates into a positive NAO response with some delay (Hinssen and Ambaum 2010), potentially affecting the 200-hPa geopotential height response presented in Figs. 2a and 2b. For the residual case (Fig. 9a) in early winter, ERA5 shows negative HF regressions, consistent with an intensification of the polar vortex in November and December, potentially supporting a positive NAO phase during that period. However, the presence of red bars in November and December suggests that the reanalysis standard error for the heat fluxes is greater than the signal itself, implying that these values in early winter are not statistically significant. The same can be argued for the total regression case depicted in Fig. 9b. A similar analysis is conducted in Fig. S9 considering directly the 100-hPa temperature between the latitudinal range of 60°–90°N.

When considering the model's outcomes in Fig. 9a, it is observed that SEAS5 fails to accurately reproduce both the intensity and the sequential pattern of heat flux seasonal evolution (Portal et al. 2022). Particularly, the December value is close to zero, and there is a lack of a pronounced sign change between early and midwinter. Although the model's ensemble mean for November aligns with the reanalysis data, it is subject to considerable variability among ensemble members, which reaches its maximum in January.

The results found in this section contrast with the findings of Hardiman et al. (2020) concerning the 2019/20 event where a strong variation in the winter's stratospheric pathways has been observed for the model. However, there may be crucial differences between examining a single event, which has specific strengths and characteristics, and the average of many.

5. Summary and conclusions

The current study explores the link between the October Indian Ocean dipole tropical SST anomalies and extratropical atmospheric circulation during the early boreal winter season. These features are summarized in Fig. 10. Notably, SST anomalies associated with the IOD in October elicit a precipitation response persisting until December. This leads to increased rainfall in the western Indian Ocean (clouds in Fig. 10) and decreased rainfall in the eastern part of the dipole (sun in Fig. 10). Subsequently, an upper-level wavenumber-3 Rossby wave is initiated (red and blue anomalies in Fig. 10). This wave, in turn, contributes to the emergence of a positive NAO pattern in December. The IOD-induced circulation response in the Euro-Atlantic sector induces a north–south precipitation dipole and a positive temperature anomaly over north-central Europe (Fig. 5).

The substantial link between October's IOD and the early winter response in the NAE regions is evident through a high correlation observed between the time series (Fig. S3) and boxplots presented in Fig. 4. To deepen the understanding of this teleconnection, the mechanisms behind the wavenumber-

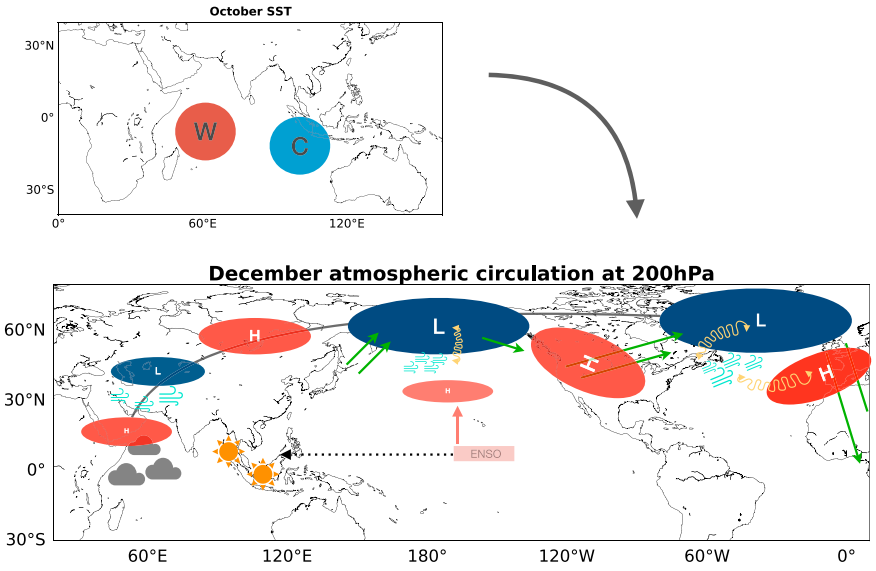

FIG. 10. Illustration depicting the mechanism behind the extratropical atmospheric circulation during early boreal winter. (top) The Indian Ocean SST pattern in October. (bottom) The December extratropical atmospheric circulation at 200 hPa. Clouds and sun symbolize the rainfall pattern over the Indian Ocean; red and blue shapes represent positive and negative 200-hPa geopotential height anomalies, respectively; green arrows depict energy propagation; the zonal wind anomalies are indicated by the sky blue heavenly lines; the yellow wavy arrows connecting winds and geopotential height anomalies represent the transient forcing positive feedback that enhances the signals.

3-like response depicted in Fig. 2a are investigated. In December, the wave originates in the South Asian region with a positive-to-negative geopotential height latitudinal dipole associated with the delayed rainfall response to a positive IOD. The wave then propagates north-eastward following the circumglobal waveguide (Branstator 2002). In the North Pacific and North Atlantic, the wave is reinforced by a positive feedback mechanism from transient eddy forcing (yellow wavy arrows in Fig. 10), which leads to a strengthening of the geopotential height responses. We speculate that this feedback is linked to a jet modification (depicted by heavenly lines in Fig. 10); however, this relationship deserves further investigation. The intensity of transients [$J(t)$] associated with the residual IOD is slightly greater than that associated with the total IOD. This suggests that ENSO plays a minor role compared to the IOD in enhancing this mechanism. This feedback is particularly strong in the North Atlantic region, where the largest magnitudes of the wave are observed. Furthermore, weak stratospheric cooling in November, associated with polar vortex strengthening, does not play a prominent role in the extratropical amplification of the wave during early winter. Moreover, enhanced energy propagation is observed over the North Atlantic and North Pacific (green arrows in Fig. 10).

The SEAS5 hindcast, while exhibiting the correct structure of the extratropical atmospheric circulation anomalies, fails to reproduce the magnitude of the signal compared to ERA5. The model displays a weaker transient eddy forcing (Fig. 6); consequently, its ability to capture extratropical atmospheric circulation is compromised. An additional explanation for the lack of signals lies in the model's limitations in simulating the early winter rainfall response to the IOD SST anomalies as shown in Fig. 7. Furthermore, the model fails to reproduce the correct intensity of the energy propagation over crucial regions such as the North Pacific and North Atlantic.

The analysis presented in this study is based on linear regression and data from the satellite period have been considered. In the future, it would also be interesting to investigate decadal changes in IOD variability (e.g., Ashok et al. 2004) and its teleconnections. Similarly, diverse IOD types have also been reported (e.g., Du et al. 2013), and such different types may also show diverse impacts on the extratropical atmospheric circulation. Also, there could be nonlinearities associated with positive and negative IOD phases, as well as with different magnitudes that could be further investigated.

Acknowledgments. The lead author would like to acknowledge the Earth System Physics (ESP) section of the Abdus Salam International Centre for Theoretical Physics (ICTP) for its support and for providing the necessary resources to conduct this study. M. A. Abid is supported by the U.K. Research and Innovation (UKRI) under the U.K. government's Horizon Europe project Grant 101081460. We also like to thank the three anonymous reviewers and the editor for their insightful comments that have improved the manuscript.

Data availability statement. For ERA5 reanalysis, visit https://cds.climate.copernicus.eu/datasets/reanalysis-era5-pressure-levels-monthly-means?tab=overview. For SEAS5, visit https://cds.climate.copernicus.eu/#!/search?text=SEAS5. All the codes used in this work are available from the corresponding author upon reasonable request.

REFERENCES

Abid, M. A., I.-S. Kang, M. Almazroui, and F. Kucharski, 2015: Contribution of synoptic transients to the potential predictability of PNA circulation anomalies: El Niño versus La Niña. *J. Climate*, **28**, 8347–8362, https://doi.org/10.1175/JCLI-D-14-00497.1.

——, M. Ashfaq, F. Kucharski, K. J. Evans, and M. Almazroui, 2020: Tropical Indian Ocean mediates ENSO influence over Central Southwest Asia during the wet season. *Geophys. Res. Lett.*, **47**, e2020GL089308, https://doi.org/10.1029/2020GL089308.

——, F. Kucharski, F. Molteni, I.-S. Kang, A. M. Tompkins, and M. Almazroui, 2021: Separating the Indian and Pacific Ocean impacts on the Euro-Atlantic response to ENSO and its transition from early to late winter. *J. Climate*, **34**, 1531–1548, https://doi.org/10.1175/JCLI-D-20-0075.1.

——, ——, ——, and M. Almazroui, 2023: Predictability of Indian Ocean precipitation and its North Atlantic teleconnections during early winter. *npj Climate Atmos. Sci.*, **6**, 17, https://doi.org/10.1038/s41612-023-00328-z.

Ashok, K., Z. Guan, and T. Yamagata, 2003: A look at the relationship between the ENSO and the Indian Ocean Dipole. *J. Meteor. Soc. Japan*, **81**, 41–56, https://doi.org/10.2151/jmsj.81.41.

——, W.-L. Chan, T. Motoi, and T. Yamagata, 2004: Decadal variability of the Indian Ocean Dipole. *Geophys. Res. Lett.*, **31**, L24207, https://doi.org/10.1029/2004GL021345.

Ayarzagüena, B., S. Ineson, N. J. Dunstone, M. P. Baldwin, and A. A. Scaife, 2018: Intraseasonal effects of El Niño-Southern Oscillation on North Atlantic climate. *J. Climate*, **31**, 8861–8873, https://doi.org/10.1175/JCLI-D-18-0097.1.

Bader, J., and M. Latif, 2005: North Atlantic Oscillation response to anomalous Indian Ocean SST in a coupled GCM. *J. Climate*, **18**, 5382–5389, https://doi.org/10.1175/JCLI3577.1.

Bladé, I., M. Newman, M. A. Alexander, and J. D. Scott, 2008: The late fall extratropical response to ENSO: Sensitivity to coupling and convection in the tropical west Pacific. *J. Climate*, **21**, 6101–6118, https://doi.org/10.1175/2008JCLI1612.1.

Branstator, G., 2002: Circumglobal teleconnections, the jet stream waveguide, and the North Atlantic Oscillation. *J. Climate*, **15**, 1893–1910, https://doi.org/10.1175/1520-0442(2002)015<1893:CTTJSW>2.0.CO;2.

Brönnimann, S., 2007: Impact of El Niño–Southern Oscillation on European climate. *Rev. Geophys.*, **45**, RG3003, https://doi.org/10.1029/2006RG000199.

Cai, W., and Coauthors, 2019: Pantropical climate interactions. *Science*, **363**, eaav4236, https://doi.org/10.1126/science.aav4236.

Chang, F.-C., and J. M. Wallace, 1987: Meteorological conditions during heat waves and droughts in the United States Great Plains. *Mon. Wea. Rev.*, **115**, 1253–1269, https://doi.org/10.1175/1520-0493(1987)115<1253:MCDHWA>2.0.CO;2.

Domeisen, D. I. V., A. H. Butler, K. Fröhlich, M. Bittner, W. A. Müller, and J. Baehr, 2015: Seasonal predictability over Europe arising from El Niño and stratospheric variability in the MPI-ESM seasonal prediction system. *J. Climate*, **28**, 256–271, https://doi.org/10.1175/JCLI-D-14-00207.1.

Du, Y., W. Cai, and Y. Wu, 2013: A new type of the Indian Ocean dipole since the mid-1970s. *J. Climate*, **26**, 959–972, https://doi.org/10.1175/JCLI-D-12-00047.1.

Fletcher, C. G., and P. J. Kushner, 2011: The role of linear interference in the annular mode response to tropical SST forcing. *J. Climate*, **24**, 778–794, https://doi.org/10.1175/2010JCLI3735.1.

——, and C. Cassou, 2015: The dynamical influence of separate teleconnections from the Pacific and Indian Oceans on the northern annular mode. *J. Climate*, **28**, 7985–8002, https://doi.org/10.1175/JCLI-D-14-00839.1.

García-Serrano, J., B. Rodríguez-Fonseca, I. Bladé, P. Zurita-Gotor, and A. de la Cámara, 2011: Rotational atmospheric circulation during North Atlantic-European winter: The influence of ENSO. *Climate Dyn.*, **37**, 1727–1743, https://doi.org/10.1007/s00382-010-0968-y.

Garfinkel, C. I., and D. L. Hartmann, 2008: Different ENSO teleconnections and their effects on the stratospheric polar vortex. *J. Geophys. Res.*, **113**, D18114, https://doi.org/10.1029/2008JD009920.

Geng, X., K.-M. Noh, K. Kim, and J.-S. Kug, 2023a: Midwinter breakdown of ENSO climate impacts in East Asia. *npj Climate Atmos. Sci.*, **6**, 155, https://doi.org/10.1038/s41612-023-00474-4.

——, J. Zhao, and J.-S. Kug, 2023b: ENSO-driven abrupt phase shift in North Atlantic Oscillation in early January. *npj Climate Atmos. Sci.*, **6**, 80, https://doi.org/10.1038/s41612-023-00414-2.

Hardiman, S. C., N. J. Dunstone, A. A. Scaife, D. M. Smith, S. Ineson, J. Lim, and D. Fereday, 2019: The impact of strong El Niño and La Niña events on the North Atlantic. *Geophys. Res. Lett.*, **46**, 2874–2883, https://doi.org/10.1029/2018GL081776.

——, ——, ——, ——, J. R. Knight, P. Davies, M. Claus, and R. J. Greatbatch, 2020: Predictability of European winter 2019/20: Indian Ocean dipole impacts on the NAO. *Atmos. Sci. Lett.*, **21**, e1005, https://doi.org/10.1002/asl.1005.

——, ——, ——, ——, R. Comer, Y. Nie, and H.-L. Ren, 2022: Missing eddy feedback may explain weak signal-to-noise ratios in climate predictions. *npj Climate Atmos. Sci.*, **5**, 57, https://doi.org/10.1038/s41612-022-00280-4.

Held, I. M., S. W. Lyons, and S. Nigam, 1989: Transients and the extratropical response to El Niño. *J. Atmos. Sci.*, **46**, 163–174, https://doi.org/10.1175/1520-0469(1989)046<0163:TATERT>2.0.CO;2.

Herceg Bulić, I., and Č. Branković, 2007: ENSO forcing of the Northern Hemisphere climate in a large ensemble of model simulations based on a very long SST record. *Climate Dyn.*, **28**, 231–254, https://doi.org/10.1007/s00382-006-0181-1.

Herceg-Bulić, I., S. Ivasić, and M. Popović, 2023: Impact of tropical SSTs on the late-winter signal over the North Atlantic-European region and contribution of midlatitude Atlantic. *npj Climate Atmos. Sci.*, **6**, 172, https://doi.org/10.1038/s41612-023-00493-1.

Hersbach, H., and Coauthors, 2020: The ERA5 global reanalysis. *Quart. J. Roy. Meteor. Soc.*, **146**, 1999–2049, https://doi.org/10.1002/qj.3803.

Hinssen, Y. B. L., and M. H. P. Ambaum, 2010: Relation between the 100-hPa heat flux and stratospheric potential vorticity. *J. Atmos. Sci.*, **67**, 4017–4027, https://doi.org/10.1175/2010JAS3569.1.

Hodson, D. L. R., R. T. Sutton, and A. A. Scaife, 2023: Signal-to-noise and predictable modes of variability in winter seasonal forecasts. *Quart. J. Roy. Meteor. Soc.*, **149**, 2598–2616, https://doi.org/10.1002/qj.4522.

Hoerling, M. P., and M. Ting, 1994: Organization of extratropical transients during El Niño. *J. Climate*, **7**, 745–766, https://doi.org/10.1175/1520-0442(1994)007%3C0745:OOETDE%3E2.0.CO;2.

Horan, M. F., F. Kucharski, N. Johnson, and M. Ashfaq, 2024: Winter precipitation predictability in Central Southwest Asia and its representation in seasonal forecast systems. *npj Climate Atmos. Sci.*, **7**, 80, https://doi.org/10.1038/s41612-024-00594-5.

Hoskins, B. J., I. N. James, and G. H. White, 1983: The shape, propagation and mean-flow interaction of large-scale weather systems. *J. Atmos. Sci.*, **40**, 1595–1612, https://doi.org/10.1175/1520-0469(1983)040<1595:TSPAMF>2.0.CO;2.

Jiménez-Esteve, B., and D. I. V. Domeisen, 2018: The tropospheric pathway of the ENSO–North Atlantic teleconnection. *J. Climate*, **31**, 4563–4584, https://doi.org/10.1175/JCLI-D-17-0716.1.

Jin, F.-F., L.-L. Pan, and M. Watanabe, 2006a: Dynamics of synoptic eddy and low-frequency flow interaction. Part I: A linear closure. *J. Atmos. Sci.*, **63**, 1677–1694, https://doi.org/10.1175/JAS3715.1.

——, ——, and ——, 2006b: Dynamics of synoptic eddy and low-frequency flow interaction. Part II: A theory for low-frequency modes. *J. Atmos. Sci.*, **63**, 1695–1708, https://doi.org/10.1175/JAS3716.1.

Johnson, S. J., and Coauthors, 2019: SEAS5: The new ECMWF seasonal forecast system. *Geosci. Model Dev.*, **12**, 1087–1117, https://doi.org/10.5194/gmd-12-1087-2019.

Joshi, M. K., M. A. Abid, and F. Kucharski, 2021: The role of an Indian Ocean heating dipole in the ENSO teleconnection to the North Atlantic European region in early winter during the twentieth century in reanalysis and CMIP5 simulations. *J. Climate*, **34**, 1047–1060, https://doi.org/10.1175/JCLI-D-20-0269.1.

Kang, I.-S., and J.-S. Kug, 2002: El Niño and La Niña sea surface temperature anomalies: Asymmetry characteristics associated with their wind stress anomalies. *J. Geophys. Res.*, **107**, 4372, https://doi.org/10.1029/2001JD000393.

——, and J. Shukla, 2006: Dynamic seasonal prediction and predictability of the monsoon. *The Asian Monsoon*, Springer, 585–612, https://doi.org/10.1007/3-540-37722-0_15.

——, J.-S. Kug, M.-J. Lim, and D.-H. Choi, 2011: Impact of transient eddies on extratropical seasonal-mean predictability in DEMETER models. *Climate Dyn.*, **37**, 509–519, https://doi.org/10.1007/s00382-010-0873-4.

King, M. P., I. Herceg-Bulić, I. Bladé, J. García-Serrano, N. Keenlyside, F. Kucharski, C. Li, and S. Sobolowski, 2018a: Importance of late fall ENSO teleconnection in the Euro-Atlantic sector. *Bull. Amer. Meteor. Soc.*, **99**, 1337–1343, https://doi.org/10.1175/BAMS-D-17-0020.1.

——, ——, F. Kucharski, and N. Keenlyside, 2018b: Interannual tropical Pacific sea surface temperature anomalies teleconnection to Northern Hemisphere atmosphere in November. *Climate Dyn.*, **50**, 1881–1899, https://doi.org/10.1007/s00382-017-3727-5.

Kucharski, F., A. Bracco, J. H. Yoo, A. M. Tompkins, L. Feudale, P. Ruti, and A. Dell'Aquila, 2009: A Gill–Matsuno-type mechanism explains the tropical Atlantic influence on African and Indian monsoon rainfall. *Quart. J. Roy. Meteor. Soc.*, **135**, 569–579, https://doi.org/10.1002/qj.406.

Li, Y., and N.-C. Lau, 2012: Impact of ENSO on the atmospheric variability over the North Atlantic in late winter–role of transient eddies. *J. Climate*, **25**, 320–342, https://doi.org/10.1175/JCLI-D-11-00037.1.

Ma, T., and Coauthors, 2022: Different ENSO teleconnections over East Asia in early and late winter: Role of precipitation anomalies in the tropical Indian Ocean and far western Pacific. *J. Climate*, **35**, 7919–7935, https://doi.org/10.1175/JCLI-D-21-0805.1.

Mayer, M., M. A. Balmaseda, S. Johnson, and F. Vitart, 2023: Assessment of seasonal forecasting errors of the ECMWF system in the eastern Indian Ocean. *Climate Dyn.*, **62**, 1391–1406, https://doi.org/10.1007/s00382-023-06985-3.

Mezzina, B., J. García-Serrano, I. Bladé, and F. Kucharski, 2020: Dynamics of the ENSO teleconnection and NAO variability in the North Atlantic–European late winter. *J. Climate*, **33**, 907–923, https://doi.org/10.1175/JCLI-D-19-0192.1.

Molteni, F., and A. Brookshaw, 2023: Early- and late-winter ENSO teleconnections to the Euro-Atlantic region in state-of-the-art seasonal forecasting systems. *Climate Dyn.*, **61**, 2673–2692, https://doi.org/10.1007/s00382-023-06698-7.

——, and Coauthors, 2011: The new ECMWF seasonal forecast system (System 4), ECMWF Tech. Memo. 656, 49 pp., https://doi.org/10.21957/4nery093i.

——, T. N. Stockdale, and F. Vitart, 2015: Understanding and modelling extra-tropical teleconnections with the Indo-Pacific region during the northern winter. *Climate Dyn.*, **45**, 3119–3140, https://doi.org/10.1007/s00382-015-2528-y.

——, and Coauthors, 2020: Boreal-winter teleconnections with tropical Indo-Pacific rainfall in HighResMIP historical simulations from the PRIMAVERA project. *Climate Dyn.*, **55**, 1843–1873, https://doi.org/10.1007/s00382-020-05358-4.

Moron, V., and I. Gouirand, 2003: Seasonal modulation of the El Niño–southern oscillation relationship with sea level pressure anomalies over the North Atlantic in October–March 1873–1996. *Int. J. Climatol.*, **23**, 143–155, https://doi.org/10.1002/joc.868.

Park, C.-H., J. Choi, S.-W. Son, D. Kim, S.-W. Yeh, and J.-S. Kug, 2023: Sub-seasonal variability of ENSO teleconnections in western North America and its prediction skill. *J. Geophys. Res. Atmos.*, **128**, e2022JD037985, https://doi.org/10.1029/2022JD037985.

Portal, A., P. Ruggieri, F. M. Palmeiro, J. García-Serrano, D. I. V. Domeisen, and S. Gualdi, 2022: Seasonal prediction of the boreal winter stratosphere. *Climate Dyn.*, **58**, 2109–2130, https://doi.org/10.1007/s00382-021-05787-9.

Rashid, I. U., M. A. Abid, M. Almazroui, F. Kucharski, M. Hanif, S. Ali, and M. Ismail, 2022: Early summer surface air temperature variability over Pakistan and the role of El Niño–Southern Oscillation teleconnections. *Int. J. Climatol.*, **42**, 5768–5784, https://doi.org/10.1002/joc.7560.

Rodó, X., E. Baert, and F. A. Comín, 1997: Variations in seasonal rainfall in southern Europe during the present century: Relationships with the North Atlantic Oscillation and the El Niño–Southern Oscillation. *Climate Dyn.*, **13**, 275–284, https://doi.org/10.1007/s003820050165.

Rowell, D. P., 1998: Assessing potential seasonal predictability with an ensemble of multidecadal GCM simulations. *J. Climate*, **11**, 109–120, https://doi.org/10.1175/1520-0442(1998)011<0109:APSPWA>2.0.CO;2.

Saji, N. H., and T. Yamagata, 2003: Possible impacts of Indian Ocean Dipole mode events on global climate. *Climate Res.*, **25**, 151–169, https://doi.org/10.3354/cr025151.

——, B. N. Goswami, P. N. Vinayachandran, and T. Yamagata, 1999: A dipole mode in the tropical Indian Ocean. *Nature*, **401**, 360–363, https://doi.org/10.1038/43854.

Scaife, A. A., and D. Smith, 2018: A signal-to-noise paradox in climate science. *npj Climate Atmos. Sci.*, **1**, 28, https://doi.org/10.1038/s41612-018-0038-4.

——, and Coauthors, 2017: Tropical rainfall, Rossby waves and regional winter climate predictions. *Quart. J. Roy. Meteor. Soc.*, **143** (702), 1–11, https://doi.org/10.1002/qj.2910.

——, and Coauthors, 2019: Does increased atmospheric resolution improve seasonal climate predictions? *Atmos. Sci. Lett.*, **20**, e922, https://doi.org/10.1002/asl.922.

Shaw, T. A., J. Perlwitz, and O. Weiner, 2014: Troposphere-stratosphere coupling: Links to North Atlantic weather and climate, including their representation in CMIP5 models. *J. Geophys. Res. Atmos.*, **119**, 5864–5880, https://doi.org/10.1002/2013JD021191.

Swenson, E. T., and D. M. Straus, 2017: Rossby wave breaking and transient eddy forcing during Euro-Atlantic circulation regimes. *J. Atmos. Sci.*, **74**, 1735–1755, https://doi.org/10.1175/JAS-D-16-0263.1.

Takaya, K., and H. Nakamura, 1997: A formulation of a wave-activity flux for stationary Rossby waves on a zonally varying basic flow. *Geophys. Res. Lett.*, **24**, 2985–2988, https://doi.org/10.1029/97GL03094.

——, and ——, 2001: A formulation of a phase-independent wave-activity flux for stationary and migratory quasigeostrophic eddies on a zonally varying basic flow. *J. Atmos. Sci.*, **58**, 608–627, https://doi.org/10.1175/1520-0469(2001)058%3C0608:AFOAPI%3E2.0.CO;2.

Thornton, H. E., D. M. Smith, A. A. Scaife, and N. J. Dunstone, 2023: Seasonal predictability of the East Atlantic Pattern in late autumn and early winter. *Geophys. Res. Lett.*, **50**, e2022GL100712, https://doi.org/10.1029/2022GL100712.

Ting, M., and I. M. Held, 1990: The stationary wave response to a tropical SST anomaly in an idealized GCM. *J. Atmos. Sci.*, **47**, 2546–2566, https://doi.org/10.1175/1520-0469(1990)047<2546:TSWRTA>2.0.CO;2.

Toniazzo, T., and A. A. Scaife, 2006: The influence of ENSO on winter North Atlantic climate. *Geophys. Res. Lett.*, **33**, L24704, https://doi.org/10.1029/2006GL027881.

Trascasa-Castro, P., A. C. Maycock, Y. Y. S. Yiu, and J. K. Fletcher, 2019: On the linearity of the stratospheric and Euro-Atlantic sector response to ENSO. *J. Climate*, **32**, 6607–6626, https://doi.org/10.1175/JCLI-D-18-0746.1.

Trenberth, K. E., G. W. Branstator, D. Karoly, A. Kumar, N.-C. Lau, and C. Ropelewski, 1998: Progress during TOGA in understanding and modeling global teleconnections associated with tropical sea surface temperatures. *J. Geophys. Res.*, **103**, 14 291–14 324, https://doi.org/10.1029/97JC01444.

van Loon, H., and R. A. Madden, 1981: The Southern Oscillation. Part I: Global associations with pressure and temperature in northern winter. *Mon. Wea. Rev.*, **109**, 1150–1162, https://doi.org/10.1175/1520-0493(1981)109<1150:TSOPIG>2.0.CO;2.

Wilks, D. S., 2016: "The stippling shows statistically significant grid points": How research results are routinely overstated and overinterpreted, and what to do about it. *Bull. Amer. Meteor. Soc.*, **97**, 2263–2273, https://doi.org/10.1175/BAMS-D-15-00267.1.

Williams, N. C., A. A. Scaife, and J. A. Screen, 2023: Underpredicted ENSO teleconnections in seasonal forecasts. *Geophys. Res. Lett.*, **50**, e2022GL101689, https://doi.org/10.1029/2022GL101689.

Yang, Y., S.-P. Xie, L. Wu, Y. Kosaka, N.-C. Lau, and G. A. Vecchi, 2015: Seasonality and predictability of the Indian Ocean dipole mode: ENSO forcing and internal variability. *J. Climate*, **28**, 8021–8036, https://doi.org/10.1175/JCLI-D-15-0078.1.

Zhang, W., and F. Jiang, 2023: Subseasonal variation in the winter ENSO-NAO relationship and the modulation of tropical North Atlantic SST variability. *Climate*, **11**, 47, https://doi.org/10.3390/cli11020047.

Zhao, Y.-B., N. Žagar, F. Lunkeit, and R. Blender, 2023: Atmospheric bias teleconnections in boreal winter associated with systematic sea surface temperature errors in the tropical Indian Ocean. *Wea. Climate Dyn.*, **4**, 833–852, https://doi.org/10.5194/wcd-4-833-2023.

Zhong, A., H. H. Hendon, and O. Alves, 2005: Indian Ocean variability and its association with ENSO in a global coupled model. *J. Climate*, **18**, 3634–3649, https://doi.org/10.1175/JCLI3493.1.